Environmental Science Nano

Biotransformations and cytotoxicity of eleven graphene and inorganic two-dimensional nanomaterials using simulated digestions coupled with a triculture in vitro model of the human gastrointestinal epithelium

Journal:	*Environmental Science: Nano*
Manuscript ID	EN-ART-06-2021-000594.R2
Article Type:	Paper

Biotransformations and cytotoxicity of eleven graphene and inorganic two-dimensional nanomaterials using simulated digestions coupled with a triculture in vitro model of the human gastrointestinal epithelium

Lila Bazina, Dimitrios Bitounis, Xiaoqiong Cao, Glen M DeLoid, Dorsa Parviz, Michael S Strano, Hao-Yu Greg Lin, David C Bell, Brian D Thrall, Philip Demokritou

Environmental Significance statement:

Human exposure to two-dimensional engineered nanomaterials (2DNMs) through ingestion may occur because of their applications in water filtration, agriculture, and medicine. Their release into soil and water bodies may also lead to their incidental ingestion by humans. However, there is little data on how 2DNMs biotransform during ingestion or how they may impact the human gastrointestinal tract (GIT). In this study, we show that ingested graphene-based and inorganic 2DNMs undergo variable physicochemical transformations in the GIT, but only WS2 causes low levels of acute cell death. Our results suggest that 2DNMs are not highly cytotoxic upon ingestion of small quantities, but their inflammatory or genotoxic potential after short- and long-term ingestion needs to be further clarified.

Biotransformations and cytotoxicity of eleven graphene and inorganic two-dimensional nanomaterials using simulated digestions coupled with a triculture in vitro model of the human gastrointestinal epithelium

*Lila Bazina[1#], Dimitrios Bitounis[1#], Xiaoqiong Cao[1], Glen M DeLoid[1], Dorsa Parviz[2], Michael S Strano[2], Hao-Yu Greg Lin[3], David C Bell[3,4], Brian D Thrall[5], Philip Demokritou[1]**

1. Center for Nanotechnology and Nanotoxicology, HSPH-NIEHS Nanosafety Research Center, Department of Environmental Health, Harvard School T.H. Chan of Public Health, Boston, MA 02115, USA

2. Department of Chemical Engineering, Massachusetts Institute of Technology, Cambridge, MA 02139, USA

3. Center for Nanoscale Systems, Harvard University, Cambridge, Massachusetts 02138, USA

4. Harvard John A. Paulson School of Engineering and Applied Sciences, Harvard University, Cambridge, Massachusetts 02138, USA

5. Biological Sciences Division, Pacific Northwest National Laboratory Richland, WA 99354, USA

Author e-mail addresses:

LB: lbazina@hsph.harvard.edu; DB: dbitounis@hsph.harvard.edu; GD: gdeloid@hsph.harvard.edu; XC: xicao@hsph.harvard.edu; DP: dparviz@mit.edu; MS: strano@mit.edu; HYGL: hlin@cns.fas.harvard.edu; DCB: dcb@seas.harvard.edu; BDT: Brian.Thrall@pnnl.gov; PD: pdemokri@hsph.harvard.edu

[#] Equally contributing first authors

*Corresponding author: Dr. Philip Demokritou

corresponding author email: pdemokri@hsph.harvard.edu

ABSTRACT

Background: Engineered nanomaterials (ENMs) have already made their way into myriad applications and products across multiple industries. However, the potential health risks of exposure to ENMs remain poorly understood. This is particularly true for the emerging class of ENMs know as 2-dimensional nanomaterials (2DNMs), with a thickness of one or a few layers of atoms arranged in a planar structure.

Methods: The present study assesses the biotransformations and *in vitro* cytotoxicity in the gastrointestinal tract of 11 2DNMs, namely graphene, graphene oxide (GO), partially reduced graphene oxide (prGO), reduced graphene oxide (rGO), hexagonal boron nitride (h-BN), molybdenum disulphide (MoS_2), and tungsten disulphide (WS_2). The evaluated pristine materials were either readily dispersed in water or dispersed with the use of a surfactant (Na-cholate or PF108). Materials dispersed in a fasting food model (FFM, water) were subjected to simulated 3-phase (oral, gastric, and small intestinal) digestion to replicate the biotransformations that would occur in the GIT after ingestion. A triculture model of small intestinal epithelium was used to assess the effects of the digested products (digestas) on epithelial layer integrity, cytotoxicity, viability, oxidative stress, and initiation of apoptosis.

Results: Physicochemical characterization of the 2DNMs in FFM dispersions and in small intestinal digestas revealed significant agglomeration by all materials during digestion, most prominently by graphene, which was likely caused by interactions with digestive proteins. Also, MoS_2 had dissolved by ~75% by the end of simulated digestion. Other than a low but statistically significant increase in cytotoxicity observed with all inorganic materials and graphene dispersed in PF108, no adverse effects were observed in the exposed tricultures.

Conclusions: Our results suggest that occasional ingestion of small quantities of 2DNMs may not be highly cytotoxic in a physiologically relevant *in vitro* model of the intestinal epithelium. Still, their inflammatory or genotoxic potential after short- or long-term ingestion remains unclear and needs to be studied in future *in vitro* and *in vivo* studies. These would include studies of effects on co-ingested nutrient digestion and absorption, which

have been documented for numerous ingested ENMs, as well as effects on the gut microbiome, which can have important health implications.

Keywords: 2D nanomaterial, graphene, graphene oxide, molybdenum disulphide, tungsten disulphide, hexagonal boron nitride, ingestion exposure, X-ray photoelectron spectroscopy

BACKGROUND

Due to their small size (at least one dimension ≤100 nm), high surface areas, and quantum phenomena, engineered nanomaterials (ENMs) possess unique physicochemical, mechanical, and optoelectronic properties compared to their bulk size counterparts [1,2]. These unique properties have enabled the development of new applications and products across multiple industries, including the construction [3], automotive [4], biomedical [5,6], toners for printing equipment [7,8], cosmetics [9], agriculture [10,11], and food industries [12–15], and their use is expected to increase in the future [16–18].

Since the discovery of graphene in 2004, interest in the development of two dimensional nanomaterials (2DNMs) has been growing exponentially [19]. Graphene provided a major advancement in the scientific community due to its intrinsic properties and potential applications [20]. Graphene is characterized as a single-atom-thick layer of graphite composed of sp^2 hybridized carbon atoms arranged in a hexagonal lattice [21]. In addition to graphene, several graphene-related materials (GRMs), in which graphene is variably functionalized with oxygen-containing moieties such as carboxyl, hydroxyl, and epoxide groups, have been developed. The most common GRMs include graphene oxide (GO), reduced graphene oxide (rGO), and partially reduced graphene oxide (prGO). GO is obtained by fully oxidizing and exfoliating graphite using strong oxidizing agents under acidic conditions. rGO and prGO are variably reduced versions of GO with lower oxygen-to-carbon ratios [22]. GRMs offer a wide variety of applications, such as biosensors, tissue engineering, drug delivery, and biomedical applications [21]. The discovery of graphene and GRMs has inspired the recent development and study of new classes of 2DNMs,

including the transition metal dichalcogenides (TMD) (e.g., MoS_2 and WS_2) and hexagonal boron nitride (h-BN) [20]. These unique nanomaterials have shown to be promising building blocks for the development of advanced drug carriers [23,24], lubricants, adhesives [25,26], and biosensors [27,28].

As new applications and production of 2DNMs continue to increase, human exposures and the associated potential health risks will inevitably occur. Exposures may be intentional, as in the case of biosensors, or unintentional, from occupational or environmental sources [18,29]. Potential routes of exposure include ingestion, inhalation, and dermal contact [30]. The proposed use of these nanomaterials in applications like water filtration [31], smart food packaging [32], and fertilizer formulations [33] could eventually lead to unintentional ingestion and exposure of the gastrointestinal tract (GIT) to 2DNMs. 2DNMs could also be transported to the GIT via mucociliary clearance and swallowing following inhalation exposure. This was demonstrated by Li et al., who concluded that inhaled nanoparticle concentrations in the lungs decreased over time as a result of mucociliary clearance, which transported the nanoparticles to the GIT, and ultimately to the faces [34].

In general, very little is known of the toxicity of ingested ENMs and even less for emerging classes of anisotropic ENM, like 2DNMs [35–38]. The majority of cellular studies that have assessed the toxicity of ENMs in the GIT have considered the toxicity of only the pristine nanomaterials dispersed in cell culture medium, neglecting the critical role that the physicochemical transformation of these materials during digestion plays in their bio-interactions, including toxicity [35]. Data from such studies is thus difficult to interpret in a physiologically relevant context. Even fewer studies have focused on the effects of ingested ENMs on gut microbiome or proteome [39–42].

As ingested 2DNMs travel through the GIT, they encounter several different surface-active molecules (such as mucin, proteins, phospholipids, and bile salts) [43–45] and distinctive biochemical milieus while they travel through three main sites which are the mouth (pH 6.7-7.0), stomach (pH 1.5 and 2.5) and small intestine (pH 6.0 to 7.0) [46]. As 2DNMs are sequentially exposed to these different environments, they are able to adsorb proteins, lipids and other molecules onto their surfaces, creating a crown-like structure commonly known as the biocorona [40,47], and to undergo transformations affecting key properties, such as shape, size, charge, surface area, agglomeration

state, and dissolution kinetics [43–45,48], all of which modulate nano-bio-interactions and thus bioactivity or toxicity [49,50]. The most common cause of toxicity for metallic ENMs is metal ions released by the dissolution of the material, which depends upon the chemical environment or environments that it encounters [50]. Recently, the increased bioavailability of ingested pesticides has been identified as a considerable source of ENM-related toxicity [51]. Another property transformation that can have profound effects on toxicity and bio-interactions is agglomeration. It has also been shown that pristine graphene oxide nanoparticles at low pH undergo significant agglomeration [52], which has been reported to impact cellular uptake; however, more data is necessary to fully understand the toxicity implications of 2DNM agglomeration in the GIT [53].

It has been shown that ingested nanoparticles can translocate across the small intestinal epithelium by either transcellular or paracellular routes depending on the size and other properties of the particle. A study by Frohlich and Roblegg showed that the most common mechanism of uptake was endocytosis [54]. It has also been shown that nanoparticles with diameters less than 100 nm are able to enter cells and that nanomaterials with diameters less than 40 nm can enter the nucleus [21]. Furthermore, rGO and prGO can adhere to the lipid bilayer cell membrane due to their hydrophobic, unmodified graphitic domains (not bound to oxygen). Accordingly, it has been suggested that chronic cellular exposure to high concentrations of graphene should be limited to prohibit physical or biological damages to the cell membrane [21]. In previous studies, the size and concentration of GO and rGO toxicity assessment against human mesenchymal stem cells (hMSCs) was assessed [19]. It was found that rGO with a 11±4 nm average lateral dimension caused significant toxicity at low concentrations; however, rGO sheets with lateral dimensions of 3.8±0.4 μm showed cellular toxicity at higher concentrations only (100 μg mL^{-1}) [19].

Furthermore, Fu et al. reported that maternal mice that were given orally a suspension with a low concentration of GO caused more damage to the intestinal tract than a higher concentrated GO suspension [53]. This discrepancy was thought to be due to increased gastric acid secretion in response to the high dose of GO, which in turn induced agglomeration of the GO nanosheets, reducing their uptake and resulting in greater clearance from the GIT [53]. In a recent *in vitro* study by our lab, which employed physiologically relevant simulated digestion and triculture

epithelium models (as in the current study but rarely used in other studies to date), GO with lateral sizes of 0.24 μm and 1.13 μm were able to induce a significant increase in reactive oxygen species generation at a starting food model (water) concentration of 250 μg/ml [55].

In vivo and *in vitro* toxicological assessments of h-BN and TMDs are very limited; Some preliminary studies have shown that these materials can induce biological toxicity. In one recent study it was shown that chemically modified and highly soluble BN with PEG (polyethylene glycol) (~10 nm) produced tissue lesions in liver, spleen, lung, and heart in mice [56]. Oral consumption of nano-molybdenum disulphide in mice was found to induce significant toxicity in the small intestine, with mucosal haemorrhage and villus shorting observed after 90 days of exposure [57]. Inflammatory markers (*TNF-α* and *MCP-1)* in the small intestine were also significantly upregulated [57].

Because of the potential for 2DNMs to undergo many and varied physicochemical transformations during digestion, it is essential that *in vitro* cellular toxicity studies be performed using materials subjected to physiologically relevant conditions that mimic the complex environment they would encounter as they progress to the GIT. In this comprehensive study on 11 industrially relevant 2DNMs, members of the graphene family, transition metal dichalcogenides, and hBN were submitted to simulated 3-phase digestion to characterize these transformations. Next, their acute cytotoxicity was assessed using a physiologically relevant *in vitro* model of the human intestinal epithelium, previously described in detail by the authors in the Deloid et al. publication [58]. This tissue model featured differentiated small intestinal enterocytes (Caco-2 cells), goblet-like columnar cells (HT29) responsible for mucus secretion, and specialized microfold cells responsible for antigen uptake and transport to the associated lymphoid tissue in the Peyer's patches of the small intestinal epithelium.

METHODS

Synthesis and size-sorting of graphene-based and inorganic 2DNMs:

Table 1 summarizes the 2DNMs and their pristine size properties, and dispersant used in this study. In summary, 3 size variants of graphene oxide (GO), 2 size variants of reduced graphene oxide (rGO), 1 partially reduced graphene oxide (prGO), 2 types of graphene, and 3 types of inorganic 2DNMs (hexagonal boron nitride, molybdenum disulphide, and tungsten disulphide) were synthesized by the authors in-house and used in this study. The dispersion of hydrophobic 2DNMS (rGO, prGO, graphenes, and inorganic 2DNMs) in water was achieved at the time of synthesis with either sodium cholate hydrate (Na-cholate, >99%, Sigma) or Pluronic® F-108 (PF108, >99%, Sigma).

In more detail:

Graphene oxide used in this study were synthesized according to a modified Hummer's method previously presented by the authors [59]. Reduced and partially reduced graphene oxides were synthesized by controlled reduction using l-ascorbic acid and size-sorted graphene oxide as the starting material. Graphene and inorganic 2DNMs (hBN, MoS_2, and WS_2) were synthesized by liquid-phase exfoliation in the presence of Na-cholate or Pluronic F108 (PF108). For all 2DNM, size sorting was performed by means of centrifugation and was certified by single-particle tracking. More detailed information on the synthesis and size-sorting of 2DNM are provided in the supplemental information section.

Physicochemical and microbiological characterization of as-synthesized graphene-based and inorganic 2DNMs:

The thickness and size distribution (lateral and hydrodynamic) of as-synthesized 2DNMs were measured by means of atomic force microscopy (AFM) and single-particle tracking (SPT). Their chemical properties were measured by inductively coupled plasma mass spectrometry (ICPMS), UV-Vis, Fourier-transform infra-red (FTIR), Raman, and X-ray photoelectron (XPS) spectroscopy. Finally, the as synthesized 2DNM suspensions were tested for microbiological sterility and endotoxin contamination. More information on the physical, chemical, biochemical, and microbiological assays performed for the characterization of the pristine 2DNMs can be found in the supplemental information.

2DNM dispersion and preparation of 2DNM-enabled food models:

Fasting food models of 2DNMs were prepared by diluting 2DNMs suspensions synthesized in HyClone™ cell culture grade water. In more detail, 20 ml of as-synthesized 2DNM suspensions were transferred to sterile, nonpyrogenic, 14 mL, polypropylene, round-bottom tubes and sonicated at 75 J/ml for 60 seconds following a protocol described in more detail elsewhere[33]. The sonicated 2DNMs suspensions were then diluted with HyClone™ cell culture grade water at final concentrations of 50 μg/ml or 250 μg/ml, thus preparing nano-enabled fasting-food models (FFMs) for the simulated digestions. Blank controls were either HyClone™ cell culture grade water (blank FFM), PF108 (blank FFM+PF108), or Na-cholate (blank FFM+Na-cholate).

Colloidal characterization of 2DNM-enabled fasting food models:

Measurements of hydrodynamic diameter (z-average), mean diffusion coefficient (D), and poly-dispersity index (pdi) of the as-prepared 2DNM 250 μg/mL were performed with a Zetasizer NanoZS by Malvern Instruments Ltd. Immediately after synthesis, 1 mL aliquots of each sample were transferred in 12 mm disposable, polystyrene cuvettes. Each sample was illuminated with a 633 nm He–Ne laser beam and D and pdi values were calculated in regular time intervals according to the ISO recommended cumulants analysis of the correlograms. For all samples, measurements were performed at 25 °C and measurement position and laser attenuation were set automatically by the instrument. The z-potential of the same 2DNM dispersions were measured with the same instrument using disposable folded capillary cells (DTS1070). All measurements were performed in triplicates.

Simulated GIT digestion of the 2DNM-enabled food models.

FFM dispersions were subjected to 3-plase (oral, gastric, and small intestinal) in vitro simulated digestion as previously described in detail and illustrated in **Figure 1** [58]. Briefly, in the oral phase, nano-enabled food models and controls were warmed to 37°C, then mixed and with pre-warmed 37°C simulated saliva, containing mucin and various salts at a pH of 6.8, and inverted by hand for 15 seconds. The resulting oral phase digesta was then combined with pre-warmed 37°C simulated gastric fluid, containing pepsin, HCl, and NaCl, at pH 2.0, and

incubated for 2 hours in a shaker at 37°C, to simulate the gastric phase of digestion. The resulting gastric phase digesta ("chyme") was then combined and mixed with bile salts, lipase, and additional mineral salts, and the pH of the mixture was adjusted to 7.0 by addition of NaOH or HCL, to simulate small intestinal fluid. The small intestinal phase mixture was incubated in a rotary shaking incubator at 37°C for 2 hours, representing the small intestinal phase of digestion [58].

Multi-angle laser diffraction measurements of oral, gastric, and small intestinal digestas:

Multi-angle laser diffraction (MALD, Mastersizer3000, Malvern Instruments, UK) was used to measure the volume-weighted size distribution of the 2DNMs small intestinal digestas at starting concentration of 250 μg/mL, as previously described by Bitounis et al. [55]. To assess the possible dissolution of WS_2 and MoS_2 across the GIT, MALD was employed to also measure their gastric and oral digestas. The soluble phase of blank FFM, blank FFM+PF108, or blank FFM+Na-cholate digestas were used to collect background measurements and correct for background noise and light refraction, as described in our previous work. In brief, the soluble phase of blank digestas was isolated by centrifugation (10 minutes at 10000×g) and the resulting supernatant was diluted 1-in-7 with HyClone™ cell culture grade water. For all samples, the instrument was set to a stirring speed of 1800 rpm and the selected particle type was "non-spherical". To enhance the accuracy of the MALD readings, the physical and optical properties of each 2DNM (namely, refractive index, absorption index, and density) were used. For each sample, light diffraction patterns were collected over 10 measurements of 120 seconds each. Following MALD measurements, volume weighted distributions were analyzed using GraphPad Prism.

X-ray photoelectron spectroscopy of 2DNMs in small intestinal digestas:

X-ray photoelectron spectroscopy (XPS) measurement was completed on the Nexsa XPS system (Thermo Scientific, Waltham, MA) to assess potential chemical changes. The probe for the measurement was aluminum K-α X-ray line with energy at 1.4866 keV and X-ray spot size was set at 400 μm. XPS data was taken after the chamber pressure was sitting at 5E-8 mBar or lower. The flood gun, which supplies both low energy electron and

ion was used throughout the entire experiment for sample surface charge compensation. Both survey spectrum and high-resolution scan were collected on both pristine and digested materials with various 2D nanomaterial (graphene oxide, MoS2 and WS2). The atomic percentages of each element and the carbon and oxygen peak deconvolution were performed by using the Thermo Scientific Avantage software. For survey spectrum, which was used to generate atomic percentages of each element, the scan was completed by taking average of 10 scans with passing energy at 200 eV and dwell time at 10 ms. For high resolution scans, the data were collected by taking average of 20 scans with passing energy at 50 eV and dwell time at 50 ms for both carbon 1s photoelectron line, which was further deconvoluted into C=C (at 283.99 eV, B.E.), C-C (at 284.72 eV, B.E.), C-S (at 286.15 eV, B.E.) and C-O (at 287.60 eV, B.E.) peaks, and oxygen 1s photoelectron line, which was further deconvoluted into O=S (at 531.19 eV, B.E.) and O-C (at 532.57 eV, B.E.) peaks. The XPS instrumental error for atomic composition is ±1%, and the accuracy of the C1s and O1s peak fitting are ±2%.

Inductively-coupled plasma mass spectrometry (ICPMS) of MoS_2 and WS_2 2DNM digestas:

The dissolution of WS_2 and MoS_2 2DNMs during simulated digestion was studied by means of ICPMS. Prior to elemental quantification, 5 ml of as-received oral, gastric, or small intestinal digestas were vortexed at high speed for 30 sec and then centrifuged at 50,000 g in a fixed-angle centrifuge for 45'. The supernatant (0.5 ml) was then carefully aspirated and diafiltrated at 14,000 g for 30' through a membrane with nominal molecular weight cut-off of 3kDa. The filtrate (400 µl) was then added in 800 µl of HyClone cell grade water and its elemental composition was quantified using a quadrupole based inductively-coupled plasma mass spectrometer (Agilent 7500ce, Santa Clara, CA 95051). HyClone cell grade water was used as a methodological blank. All samples were measured in triplicates.

Toxicological assessment of ingested 2DNMs in an *in vitro* triculture intestinal epithelial model.

Development and methods for preparing the triculture small intestinal model (**Figure 1**) were previously described by Deloid *et. al* [58]. Hypertetraploid Caco-2 epithelial cells were of human Caucasian colon adenocarcinoma origin. HT29-MTX epithelial human colon cancer cells were of unspecified karyotype. Caco-2

and HT29-MTX cells were grown in DMEM (high glucose) supplemented with 10% heat-inactivated fetal bovine serum (FBS, Sigma-Aldrich), 10 mM HEPES buffer, 100 IU/ml Penicillin, 100 µg/ml Streptomycin, and non-essential amino acids (1/100 dilution of 100 x solution, ThermoFisher, Waltham, MA). Diploid Raji B (Burkitt′s lymphoma) cells were cultured in suspension in RPMI 1640 + 10% FBS, 10 mM HEPES buffer, 100 IU/ml Penicillin and 100 µg/ml Streptomycin. All cell lines were obtained from Sigma-Aldrich Corp, St. Louis, MO. Caco-2 and HT-29MTX cells were trypsinized and resuspended in DMEM media at 3×10^5 cells/cm^3. They were then combined at a ratio of 3:1 (Caco-2:HT29-MTX) and 1.5 ml of the cell mixture was seeded on polyester transwell inserts with 0.4 µm pores fitted in 6-well transwell plates. Inserts and plates were purchased from Corning (Corning, NY). The basolateral compartments of the transwell plates were filled with 2.5 ml of complete medium. Media was changed after four days and subsequently every other day until day 15. On days 15 and 16 basolateral media was replaced with 2.5 ml of Raji B cells at a concentration of 1×10^6 cells/ml in 1:1 DMEM: RPMI complete media. For 96-well plates, Caco-2 and HT-29MTX cells at a 3:1 ratio were seeded at 3×10^4 cells/well (100 µl of cell mixture) in Black-walled, clear optical bottom plates (BD Biosciences, Billerica, MA). Media was changed after four days and subsequently every other day until day 17. Toxicology experiments were initiated on day 17.

Exposure of tricultures to 2DNM digestas

The final digestas from simulated digestions were mixed with phenol red-free DMEM without FBS at a ratio of 1:3. The resulting mixture was applied to the cells (1.5 ml to the apical compartments of transwell inserts and 200 µl per well in 96-well plates). The apical fluid in untreated control wells, and the media in 96-well controls was replaced with fresh media.

Cytotoxicity assessment

Transepithelial electrical resistance (TEER), a measure of epithelial barrier and cell junctional integrity, was measured using an EVOM2 Epithelial Volt/Ohm Meter with a Chopstick Electrode Set (World Precision Instruments, Sarasota, FL) immediately before and 24 hours after digesta exposures.

LDH release (plasma membrane damage) was measured in transwell tricultures after 24 hour digesta exposures using the Pierce LDH assay kit (Sigma Aldrich, St. Louis, MO) according to the manufacturer's instructions as previously described in detail by the authors [38].

Oxidative stress (production of ROS) was assessed in 96-well plates using the CellROX® green reagent (Thermo Fisher, Waltham MA) according to the manufacturer's instructions as previously described by the authors [38].

Viability (mitochondrial enzyme activity) was assessed in 96-well plates using the PrestoBlue™ Cell Viability Reagent (ThermoFisher, Waltham MA) according to the manufacturer's instructions. Following 24 h exposures, cells were washed 3 times with PBS and 100 µl of a 10% working solution of the PrestoBlue reagent (diluted in DMEM without phenol red) was added to each well. Plates were incubated at 37 °C, 5% CO_2 for 15 minutes and fluorescence was measured at 560 nm (excitation)/590 nm (emission).

Apoptosis was assessed in 96-well plates after 24 h exposures using the CellEvent Caspase-3/7 Green Detection kit (ThermoFisher) according to the manufacturer's instructions. Briefly, co-cultures grown in 96-well plates were washed twice with pre-warmed PBS and incubated with 200 µl/well of either digesta or media containing 0.25 µM staurosporine (positive control, induces apoptosis, Sigma) at 37 °C and 5% CO_2 for 24 hours. Cells were then washed twice with pre-warmed PBS before 100 µl of an 8 µM working reagent solution (diluted from 2.0 mM stock in PBS with 5% FBS) was added to the wells. The 96 well plates were then incubated for 45 min at 37 °C and 5% CO_2, washed once with warm PBS, and incubated with 100 µl of 4% formaldehyde at room temperature for 15 minutes. The formaldehyde was then replaced with 200 µl of room temperature PBS and fluorescence was measured at 502 nm (excitation)/530 nm (emission). Apoptosis activity was calculated by first subtracting the background values (measurements from untreated, unstained wells) from the values of unknown samples, then normalizing the background-corrected measurements to the stained negative control values and expressing the result in fold-change. Interferences from 2DNMs with the Pierce LDH assay kit, CellEvent Caspase-3/7 Green Detection kit, PrestoBlue™ Cell Viability Reagent, and CellROX® green reagent were tested as presented in the supplementary methods and **Figure S1**.

Statistical analysis. Experiments were performed in triplicates and statistical analyses were performed on GraphPad© Prism version 8.4.3 software (GraphPad Software, Inc., San Diego, CA) using two-way ANOVA tests and multiple comparisons (corrected with Dunnett's test); and unpaired t tests (nonparametric).

RESULTS

Physicochemical and biological properties of 2DNMs

Table 1 presents a summary of key properties of as-synthesized 2DNMs, including the thickness, lateral size, C:O ratio for graphene-related materials, and the concentration of either the Na-cholate or PF108 used to disperse the hydrophobic 2DNMs. The complete morphological, physicochemical, and biological characterization of as-synthesized hBN, MoS_2, reduced graphene oxide (rGO-S), and small-sized graphene dispersed in Na-cholate (g-Na-cholate-S) can be found in a recent publication by Duan et al. [60]. The complete morphological, physicochemical, and biological characterization of as-synthesized medium- and large-sized GO have been presented in a previous publication by the authors [55]. **Tables S1-S6** present full characterization data (morphological, physicochemical, and biological) on the small variant of graphene oxide (GO-S), small-sized graphene dispersed in PF108 (g-PF108-S), reduced graphene oxides (rGO-S, rGO-L), partially reduced graphene oxide (prGO), and tungsten disulphide (WS_2).

Colloidal characterization of 2DNM-enabled fasting food models

Right after preparation, 2DNM-enabled fasting food models were measured by dynamic light scattering (DLS) and electrophoretic light scattering. **Table 2** summarizes the measured colloidal properties, including z-average hydrodynamic diameter, polydispersity index, z-potential, and diffusion coefficient. In brief, all samples presented with a narrow pdi which indicates successful size-sorting and good nano-sheet size homogeneity within each sample. Increasing particle size as measured by microscopy techniques (see supporting information tables S1-S5) were in accordance with increasing hydrodynamic size (z-average) and decreasing diffusion coefficient

values. The colloidal stability of all samples was verified by large z-potential values which generally ranges from -35 to -47 mV, except for graphene in Pluronic F108, which was acceptable at -16 mV. Overall, 2DNM-enabled fasting food models presented good colloidal stability prior to their simulated digestion.

Physicochemical transformations of 2DNMs across the simulated gastrointestinal tract

Chemical Transformations

Figure 2 presents the XPS analyses of 2DNM-enabled fasting food models before and after simulated digestion. It was previously shown by the authors that GO-M and GO-L are reduced upon digestion as manifested by an overal increase in C-N content and restoration of sp^2-hybridized C-C bonds [55]. As presented in **Figure S2**, GO-S underwent similar chemical transformations. In contrast, reduced and partially reduced graphenes maintained the same C:O atomic ratio (~0.3), suggesting that they do not undergo further reduction upon simulated digestion, as shown in **Figure 2A-C**. At the same time, a significant amount of nitrogen is added to the sample (N/C ~ 0.10 - 0.12 in all rGO-S, rGO-L, and prGO). In the case of inorganic 2DNMs and, in particular, MoS_2 the only significant change is in the ratio of MoO_3/MoS_2 in the sample, as shown in **Figure 2D**. Before digestion, 15% of Mo is present as MoO_3, mainly due to oxidation in presence of water and air. In the small intestinal digesta, contribution from MoO_3 decreases to ~10%, indicating the sulfurization of some MoO_3. When it comes to WS_2, a considerable decrease in oxidized tungsten (WO_3) is observed in the small intestinal digesta, both in terms of peak intensity and negative shift in binding energy of WO_3 peaks, as shown in **Figure 2E**. This is also confirmed by reduction of O-W peaks in O1s spectra. At the same time, the ratio of S/W is increased after digestion.

Dissolution of transition metal dichalcogenide 2DNMs

The results of dissolution evaluation by means of ICPMS for the transition metal dicalcogenide 2DNMs MoS_2 and WS_2 during simulated digestion are summarized **Figure 3**. MoS_2 particles underwent 29% and 15% dissolution during the oral and gastric phase, respectively, and further dissolved by 30% after the small intestinal phase. After digestion, ~75% of MoS_2 was in soluble form (**Figure 3A**). In contrast, WS_2 only dissolved by ~2%

throuhgout the oral and gastric phases, but by the end of the small intestinal phase, WS_2 had dissolved by an additional 15%. After digestion, ~20% of WS_2 was in soluble form (**Figure 3B**).

Size transformations of 2DNMs during digestion

Size distributions of test 2DNMs in FFM dispersions (water) and small intestinal digesta, assessed by MALD, are summarized in **Figure 4**. The size transformations the three GO size variants are shown in Figure **4A-4C**. The volume-weighted size distributions of FFM dispersions of GO-S and GO-M, included significant nanoscale components with peaks at ~80 and 100 nm respectively, whereas that of GO-L did not. Dispersions of all three GO materials had peaks in the 10-100 μm range, which increased in size from small to large size GO. Dispersions of all three materials also included a fraction in the 0.5-1.5 mm, which was largest in the GO-M dispersion. In contrast to the starting FFM dispersions, the digestas of these GO dispersions all had nearly identical polydisperse size distributions with broad peaks stretching from ~1 μm to 1 mm. These GO-FFM digesta distributions were less broad and had larger components in the 1-10 μm range, but smaller components in the nanoscale range. The result was an overall shift to larger sizes, which is confirmed by comparing the sizes (diameters) at which the 10^{th}, 50^{th}, and 90^{th} percentiles of the volume weighted size distributions (D_v10, D_v50 and D_v90) occur (**Figure 4L**). The greatest differences between the FFM blank are seen in the 90^{th} percentile sizes, which are significantly greater in GO digestas than in the blank FFM digesta.

The size distributions of FFM dispersions and digestas of reduced graphene oxide, partially reduced graphene oxide (Figure 4F), and graphene (stabilized in either sodium Na-cholate or Pluronic F108) are shown in **Figure 4D-4H**. The size distributions of all these materials, unlike the GO materials, were almost exclusively in the nanoscale range, with peaks centered at ~10 nm. The size distributions of the digestas of graphene and reduced graphene oxide forms contained broad distributions that ranged from wide monomodal peaks centred at 8-10 μm for both rGO and prGO materials to a broader and somewhat multimodal distribution from 50 nm to 800 μm for graphene stabilized in Na-cholate, and an even broader multimodal distribution from 50 nm to 1 mm for graphene stabilized in Pluronic F108. Unlike GO materials, the size distributions in the digestas of the reduced graphene

oxide materials were not right shifted relative to the corresponding controls (FFM+Na-cholate), which is consistent with the lack of differences in D_v90 (**Figure 4L**). In the case of prGO, the digesta size distribution was centered slightly to the right of that for the FFM+Na-cholate digesta control, resulting in a slightly but significantly larger D_v90 value (Figure 4L). The size distributions of the graphene digestas were more strongly right shifted, resulting in substantially and significantly larger D_v90 values in the presence of the material.

Size distributions of starting dispersions and digestas of hBN and the TMDs, MoS_2 and WS_2, are shown in Figure **4I-K**. For hBN (stabilized in Na-cholate), the results were similar to those for rGO and prGO materials, i.e., a nanoscale distribution in the starting food model (FFM+Na-cholate) with a peak at ~100 nm, and a broad distribution from ~1-100 μm after digestion, which did not differ significantly from that of the blank food model control. The size distribution of the starting MoS_2 (stabilized in Na-cholate) distribution was bimodal with peaks at ~60 nm and 10 μm. The MALD distribution of the MoS_2 digesta revealed a monomodal polydisperse system with a peak at ~5 μm, similar to that of the rGO materials. Also as with the GO materials, there were no significant differences between the D_v90 values of the digestas with and without test material. Finally, the MALD distribution of WS_2 (stabilized in Pluronic F108) was monomodal albeit with a wide distribution from ~100 nm to ~1 μm.

For the TMD 2DNMs (MoS_2 and WS_2), in addition to the small intestinal phase digesta, size distributions in oral and gastric phases were also assessed. The size distributions of MoS_2 and WS_2 in each phase of simulated digestion (compared with control digestions without material) are shown in **Figure 5.** For both materials, the size distributions in the oral phase (after incubation with mucin and amylase in artificial saliva solution) were substantially different than those in FFM dispersion (**Figure 4J and 4K**). In the case of MoS_2 (**Figure 5A**), the nanoscale component seen in FFM dispersion was not present, and sizes were distributed in a broad peak between 1 and 100 μm, which was substantially right shifted compared to that of the corresponding oral phase control (FFM+Na-cholate), as indicated by the significantly greater D_v90 value in the presence of MoS_2 (**Figure 5G**). In the case of WS_2, the single peak from ~100 nm to ~1 μm seen in FFM dispersion (**Figure 4K**) was replaced in the oral phase digesta by a bimodal distribution with two broad peaks centred at ~100 nm and ~10 μm, and the

presence of WS2 appeared to have had little effect on the distribution in that phase (**Figure 5D**), which is confirmed by a lack of significant change in D_v90 (**Figure 5G**).

In the gastric phase the MoS_2 and WS_2 digesta size distributions (**Figure 5B and 5E**) were not substantially changed relative to those in the oral phase. The right shifting effect of the presence of MoS_2 on the distribution is however less notable in this phase, although it is still statistically significant (**Figure 5I**). In the small intestinal phase, the size distribution in the presence of MoS_2 was shifted to the left with a peak at ~5 μm and differed from the control digesta (FFM+PF108) distribution, which though about equally broad and centred at ~5 μm was clearly bimodal with a more substantial smaller component. As a result, the Dv90 value in the presence of WS2 was significantly greater than in its absence (**Figure 5I**).

Toxicological assessment of 2DNMs in the GIT.

The cytotoxicity of 2DNMs was assessed at starting (food) concentrations of 50 μg/ml and 250 μg/ml using standard toxicological assays for cell viability (cellular reductase enzyme activity, PrestoBlue assay), cytotoxicity (membrane damage and LDH release), and oxidative stress (ROS generation, CellROX assay) using a tri-culture (transwell) or co-culture (96-well) small intestinal epithelium model. In addition, we assessed apoptosis (caspase 3/7 activity) at the higher starting 2DNMs concentration (250 μg/ml). It should be noted that the small intestinal phase digesta/media suspensions applied to cells are diluted by a total factor of 1/48 relative to the starting (food) concentrations, because of the GIT digestion. The cells were thus exposed to 2DNMs at concentrations of approximately 1 μg/ml and 5 μg/ml (corresponding to starting concentrations 50 μg/ml and 250 μg/ml, respectively). It also has to be mentioned that interference tests were performed and showed that the panel of 11 graphene and inorganic 2DNMs do not generate false positive results regarding their acute cytotoxicity against the *in vitro* tri-culture model of the human small intestinal epithelium studied here. As established in the literature, the cytotoxic potential of nanomaterials with possibly interfering spectroscopic and/or fluorescent properties need to be tested with multiple assays[61,62]. To that end, we evaluated 2DNM cytotoxicity using 3 distinct assays, each one based on differing endpoints, as discussed below.

Results of the toxicological assessment of ingested GO-S, GO-M, GO-L, rGO-S, rGO-L, prGO, graphene-Na-cholate, and graphene-PF108, h-BN, MoS_2 and WS2 are shown in **Figure 6**. Because the stock suspensions of all but the GO 2DNMs were stabilized by either Na-cholate or PF108 surfactant, controls included digestas of either Na-cholate alone or PF108 alone at concentrations corresponding to their highest concentrations among the 2DNM-enabled FFM suspensions.

None of the tested 2DNMs or surfactant controls caused a significant decrease in TEER relative to the FFM digesta treated samples (**Figure 6A**), suggesting that the ingested 2DNMs did not impair intestinal barrier function. At a starting FFM concentration of 50 μg/ml, rGO-L, rGO-S, hBN, and MoS2 caused slight (<5%) but statistically significant ($p < 0.05$) elevations in LDH release compared to their respective controls. However, no significant increase was observed for any of these materials at the 250 μg/ml starting concentration (**Figure 6B**). Moderate increases in LDH were observed in cells treated with digestas of graphene-PF108 and WS_2 (14%, $p<0.005$) at 250 μg/ml.

Except for rGO (small) at starting concentration of 250 μg/ml, which caused a slight but statistically significant ($p<0.05$) decrease, none of the materials had a significant effect on cell viability (mitochondrial enzymatic activity) compared to corresponding FFM, FFM/Na-cholate or FFM/PF108 controls. Likewise, none of ingested 2DNMs, at starting concentrations 250 μg/ml, caused a significant increase in caspase 3/7 activity, indicating that they did not activate the apoptotic death pathway (**Figure 6D**). Finally, most tested 2DNMs (except for GO-M and GO-L) did not induce severe oxidative stress at either starting concentration compared to corresponding controls (**Figure 6E**) with GO-M and GO-L causing small (+20%), but statistically significant ($p<0.05$) increases in ROS generation compared to the FFM control.

DISCUSSION

Colloidal characterization of 2DNM-enabled fasting food models

The 2DNMs used in this study were either readily dispersed in water due to their amphiphilicity (GO-M and GO-L) or required the use of dispersants because of their hydrophobicity (graphenes, reduced GO, partially reduced GO, and inorganic 2DNMs). The use of dispersants is necessary for the exfoliation of 2DNMs in aqueous media and their stable dispersion [63–65]. As a result, the dispersant coating around hydrophobic 2DNMs becomes an inherent property of their surface chemistry and morphology. In this study, Na-cholate was employed to disperse one graphene variant, reduced GO, partially reduced GO, and MoS_2. Na-cholate is an ionic surfactant that consists of polar and non-polar regions with the latter interfacing with the hydrophobic regions of 2DNMs. Its ionic side then interfaces with water molecules and thus increases the particles' dispersibility in water [66]. Pluronic F108 was used to disperse another graphene variant and WS_2. PF108 is a non-ionic surfactant which still has a hydrophilic and hydrophobic region [66]. The association of the hydrophobic region of PF108 with the surface of graphene and WS_2 allows the hydrophilic region to increase their aqueous dispersibility. Furthermore, the large molecular weight of PF108 provides colloidal stability by means of steric hindrance of particle aggregation [67].

The colloidal characterization of 2DNM-enabled fasting food models returned low polydispersity indices (PDIs) for all samples. Such low PDIs were expected after the rigorous size-sorting applied during the synthesis of these materials (please see Materials and Methods for more information). The cumulants analysis algorithm was then employed to calculate z-average values which correspond to the mean hydrodynamic radii of spheres with the same diffusion coefficient (D) as the observed particles. While it is not intuitive to ascribe spherical properties to 2DNMs with very large aspect ratios, D values can still be used to probe the colloidal behavior of anisotropic nanoparticles in suspension [68]. For the 2DNMs used in this study, D values negatively correlated with their lateral dimensions measured using electron and atomic force microscopy, in accordance with what others have shown [69,70]. We have previously shown that GO-M- and GO-L-enabled fasting food models are colloidally stable and do not readily agglomerate [55]. Similarly, GO-S presented with strongly negative z-potential values suggesting exceptional stability. With either surfactant, 2DNMs also achieved negative z-potential values and could be efficiently dispersed in the aqueous-based fasting food model.

Overall, light scattering experiments showed that all 2DNM-enabled FFMs were well-dispersed. Consequently, any agglomeration in the small intestinal digestas could be attributed to food matrix effects and the biochemical micro-environment of the GIT, as discussed in the next section. It is important to note here that the dispersibility of 2DNMs directly affects their biocompatibility *in vitro* [71,72]. Therefore, their dissolution, cellular uptake, and associated biological effects in the GIT should be considered contingent on the presence and nature of surfactants and always accompanied by appropriate methodological controls, as thoroughly discussed in a review article by McClements et al. [44]. In parallel, surfactants on the surface of 2DNMs are bound to mediate their interaction with the food matrix and thus influence their bioactivity, and future studies should address such effects using standardized food models representing variable dietary habits.

Physicochemical transformations of 2DNMs across the simulated gastrointestinal tract

physicochemical and morphological trasnformations of ingested nanoparticles are due to multifactorial processes that depend on the food matrix and the surface functionaliteis of the particles [35]. In the case of 2DNMs, interactions with bile salts and digestive enzymes may drastically change the entire chemical composition of the particle. In turn, the extremely high SSA of 2DNMs increases the available sites for chemical reactions. In this study, XPS was employed to identify chemical transformations to all O-containing 2DNM. XPS was not performed on ingested graphene or hBN. Graphene only has a C-C peak which are also present in Na-cholate and Pluronic F108, hence any changes before and after ingestion cannot be accurately attributed to graphene or surfactants. In the case of hBN, its B and N peaks are are not covalently functionalized and any C-containing peaks belong to Na-cholate and could not be identified as funtional groups obtianed over digestion. For the 2DNM assessed by XPS, it was found that reduced or partially reduced GO do not undergo further reduction during simluated digestion, in contrast to GO which can be reduced, in agreement to our previous findings [55]. This is probably due to the fact that most functional groups with minimal energy barrier toward reduction are already removed from the nanomaterial surface upon synthesis. Interestingly, reduction is concurrent with increase in N-content. The

deconvolution of C1s spectra in rGO-S, rGO-L, and prGO does not reveal a specific trend or mechanistic pattern related to nitrogen inclusion. However, obvious decrease in O-C=O peaks emphasize the role of carboxyl groups amidification reactions in all samples, and particularly in the case of prGO. Having said that, it is also possible that N-containing species be physisorbed on the surface, without affecting the O-containing functional groups. Unfortunately, the presence of protein corona complicates the disctinction between chemisorbed and physisorbed N. Interestingly, P is present in all rGO-S, rGO-L, and prGO at ~1 at%, even though it was not previosuly detected in digested GO. A possible reason for this difference between such close-related graphene-family materials could be the presence of dispersant necessary to stabilize the hydrophobic rGO-S, rGO-L, and prGO. Conceivably, the composition and conformation of the protein corona would be different from those in GO samples, explaining the more intensive N inclusion and presence of P. Finally, it has to be noted that some S is observed in rGO after the small intestinal phase, however S is a common impurity in GO synthesis so that it is not possible to pinpoint its origin.

In the case of MoS_2, a hard protein corona that contains S may be sulfurized in acidic environment, thus explaining the obtained XPS spectra. Still, it would require proteomic analysis in future studies to confirm this hypothesis. Regarding WS_2, the less stable WO_3 seem to undergo some redox reactions that causes the release of elemental W from crystal structure. Alternatively, sulfurization of WO_3 to WS_2 could also explain the observed spetra, assuming the protein corona contains S.

The dissolution of MoS_2 and WS_2 across the oral, gastric, and small intestinal digestion phases was assessed by means of ICPMS. hBN is known to resist oxidation and was found to resist enzymatic biodegradation [73,74], therefore its dissolution was not considerd by ICPMS. The same technique cannot be employed for C-containing GRMs and was therefore not employed to study their degradation due to ingestion. Still, graphene has been shown to be chemically inert and cannot be further reduced [75], while its oxidation requires considerably more acidic and oxidative conditions than those in the gasrtic environment [59]. It was found that MoS_2 transforms from the solid to the dissolved phase across all three simulated digestion phases (gastric, oral, and small intestinal). Its dissolution

in the gastric phase agrees with findings from a previous work by Wang et al. who showed that in oxygen saturated water and acidic pH MoS_2 nanosheets produce molybdate ion (MoO_4^{2-}) [76]. Dissolution is further accelertaed in more complex media, like cell growth media. In the current work, the kinetics of MoS_2 dissolution were faster which can be attributed to the higher concentration of salts in the FFM and alternation between peri-neutral and acidic pH. MoS_2 degradation could be further increased due to the presence of MoO_3, which has been shown to dissolve with increasing pH values [77]. Regarding WS_2, to the best of our knowledge there are no data on its biodegradability in simulated biological fluids [78]. The current study is the first to follow its biotransformation in conditions that mimick the biochemical environment of the human GIT. WS_2 nanosheets were found to partially dissolve in the slightly alkaline environment of small intestinal phase, which agress with their slow dissolution in PBS (pH 7.4), as observed by others [79]. The co-presence of other ions may have been responsible for increasing the solubility of WS_2.

Eventually, about 20% w/w of WS_2 and 75% w/w of MoS_2 were solubilized at the end of the 3-phase digestion. The size distributions of GO dispersions in FFM (**Figure 4A-C**) indicate two populations of agglomerates in the 10-100 nm and 0.5-1.5 μm ranges. The absence of a nanoscale population in the GO-L dispersion suggests that most of the material present was incorporated in agglomerates and little if any of the material existed as individual free flakes. The polydisperse distribution seen after digestion is consistent with incorporation of the materials in agglomerates of all sizes within that range regardless of the lateral size of GO. This is likely due to the large surface area and hydrophilic nature of GO, allowing it to adsorb proteins (mucin, pepsin, amylase, lipases, proteases) and other biomolecules during digestion and increasing the average size of agglomerates relative to the blank FFM control. These findings agree with agglomeration observed across the GIT for similarly sized GO used in the study by Bitounis et al. [55].

Unlike GO, the hydrophobic graphene-related materials (both sizes of rGO, prGO, and graphene) and hBN did not form agglomerates in water (FFM) owing to the presence of surfactants, as indicated by their monomodal size distributions with peaks in the nanoscale domain (**Figure 4D-I**). MoS_2, on the other hand, did form agglomerates

in water, as indicated by its bimodal distribution (**Figure 4J**), as did WS_2, evinced by its single peak in the μm size range (**Figure 4K**).

The differences in agglomeration potential among the different 2DNMs likely results from differences in the balance between attractive forces (e.g., van der Walls) and repulsive/dispersive forces due in turn to differences in surface chemistry and other physicochemical properties. It has been reported for example that rGO and prGO are relatively more stable in aqueous suspension due to the presence of polar oxygen groups, and that graphene has a greater potential to agglomerate in solution than oxidized forms due to strong van der Waals interactions.[40] As a result of these physicochemical differences, we would expect graphene to be more extensively agglomerated in digestas than prGO and rGO materials.

Toxicological assessment of 2DNMs in the GIT.

In summary, the 2DNMs investigated in this study caused little or no cytotoxicity to a physiologically relevant triculture small intestinal epithelial model. It is worth noting that this is one of only a few studies that took into consideration the bio transformations of 2DNMs in the GIT and coupled an advanced tri-culture cellular model with simulated digestions. In the absence of exposure data to 2DNMs, their starting doses in FFM at 50 or 250 μg/ml were based on the use of GO in water filtration and its possible incidental release to drinking water, as described in detail in our previous study [55]. None of the materials, at either 50 or 250 μg/ml (starting concentration in FFM, corresponding to 1 and 5 μg/ml applied to cells), produced significant or notable effects on TEER, cell viability, or caspase 3/7 activity (apoptosis) (**Figure 5**). It has to be mentioned that interference tests were performed and showed that the panel of 11 graphene and inorganic 2DNMs studied here do not generate false positive results regarding their acute cytotoxicity against the *in vitro* tri-culture model of the human small intestinal epithelium. As established in the literature, the cytotoxic potential of nanomaterials with possibly interfering spectroscopic and/or fluorescent properties need to be tested with multiple assays . To that end, we employed 3 distinct cytotoxicity assays that produce differing endpoints, as discussed below.

At 50 μg/ml, rGO-L, rGO-S, hBN, and MoS_2 caused very slight (<5%) elevations in LDH release compared to corresponding controls, but did not affect LDH release at 250 μg/ml. This discrepancy may be due to minor baseline differences between the transwell tri-cultures used to test the materials at the different concentrations, which in turn may have resulted from differences in cell passage number or other factors that can affect growth and maturation of the triculture and coculture intestinal epithelium. Small increases in LDH were also observed in cells treated with digestas of graphene-PF108, while GO-M and GO-L produced slight but statistically significant increases in ROS generation, suggesting some level of oxidative stress. WS_2 at the highest dose caused moderate toxicity in the form of 14% cell death ($p<0.005$). While the toxicity of WS_2 nanosheets is still under investigation by the scientific community, tungstate ions have been recently identified as potentially toxic with single-ppm LD_{50} against guppies (*Poecilia reticulate*) [80] as well as pronounced tumorigenicity and genotoxicity *in vitro* [81]. Given the increased dissolution of WS_2 in the current study, it is conceivable that released tungstate ions be responsible for the observed cytotoxicity. Further mechanistic studies are needed to understand the role of potential uptake and internalization of 2DNMs in cytotoxicity. In agreement to our findings, oxidative biodissolution of MoS_2 nanosheets at concentrations 10x higher than those used in the current study has been found to release levels of ionic Mo species which were non-toxic against murine macrophages or human lung epithelial cells [76]. Still, the effect of MoS_2 dissolution seems to be cell-dependent as recently hexavalent Mo was suggested as the potetnial culrpit for MoS_2 nanosheet toxicity agaisnt KUP5 cells [82].

Overall, under the experimental conditions employed in this study, graphene-related 2DNMs dispersed with or without surfactants and with variable oxidation state and lateral size present low cytotoxicity against an in vitro tri-culture model of the small intestinal epithelium. Among the inorganic 2DNMs, only WS_2 incurred low (~14%) acute cell death at the highest employed dose. Still, it should be noted that the tested materials cannot be regarded as safe and further biological studies are needed. These include inflammogenicity and genotoxicity studies as well as studies of the effects of the ingested 2DNMs on digestion and absorption of nutrients, on intestinal metabolism, and on the gut microbiome composition and function. Finally, chronic feeding studies in animal models should

also be performed to better understand the safety profile of 2DNMs and their potential adverse effects upon acute or long-term exposure through ingestion.

Despite the apparent lack of acute cytotoxicity of ingested 2DNMs, further studies are needed. Indeed, the adverse effects of ingested ENMs may be due to their interaction with the food matrix and the formation of biologcially active biocoronas [35]. For example, the formation of a biocorona around 2DNMs may impact the bioavailability of micro- and macro-nutrients. This was recently suggested as a potential mechanism responsible for the increased bioavailability of carbohydrates in the presence of nanocellulose [83]. Interaction of 2DNMs with mucin may also affect the viscosity of the intestine mucosa [84] which may framatically alter the diffusion of nutrients. Such results put into perspective studies on the effect of 2DNMs on intestinal inflammation and metabolism as well as on the gut microbiome composition and function before their safety should be declared or even regarded likely.

CONCLUSIONS

In this study, the physicochemical, morphological transformations of ingested 2DNMs, namely GO (small, medium, and large), rGO (small and large), prGO, h-BN, MoS_2, and graphene in the digestive tract were examined using a 3-stage GIT simulator. Following simulated intestinal digestion, all GO nanomaterials were observed to agglomerate when compared to the blank digesta. Such morphological changes can be attributed to agglomeration of the GO flakes due to their interaction with proteins and other biomolecules compounded by the acidification of the GIT in the gastric phase. Hydrophobic 2DNMs in Na-cholate (except graphene) avoided agglomeration following digestion with changes in relative particle size in small intestinal phase digestas compared to blank were minimal. Based on these results, Na-cholate could be responsible for nanomaterial's stability and agglomeration resistance. However, graphene in Na-cholate showed high agglomeration and the highest fold change compared to the nanomaterials in surfactant and blank. According to physicochemical properties of graphene, graphene has the highest ability to agglomerate compared to rGO and prGO that have oxygen containing functional groups. Finally, 2DNMs toxicity was assessed using a cellular *in vitro* triculture model

representing the gut epithelium coupled with simulated digestions. Based on the tested toxicity endpoints, most ingested 2DNMs lacked acute cytotoxicity at 1 μg/ml and 5 μg/ml with only WS_2 causing moderate cell death at the highest dose. Certainly, additional short- and long-term studies are required to fully comprehend their pathogenicity.

In future studies, other biological endpoints beyond cytotoxicity as well as chronic *in vivo* studies are needed to further understand potential health risks from ingested 2DNMs including studies to assess potential effects on digestion and absorption of micro and macro nutrients and effects on gut microbiome.

LIST OF ABBREVIATIONS

GIT: gastrointestinal tract, ENM: engineered nanomaterial, iENMs: ingested engineered nanomaterial, GRAS: generally regarded as safe, DLS: dynamic light scattering, FBS: fetal bovine serum, TEM: transmission electron microscopy, SEM: scanning electron microscopy, ICP-MS: inductively coupled plasma mass spectroscopy, SAR: structure activity relationship, sp-ICPMS: single particle inductively coupled plasma mass spectroscopy,

DECLARATIONS

Ethics approval and consent to participate

Not applicable.

Consent for publication

Not applicable.

Availability of data and material

The datasets used and/or analysed during the current study are available from the corresponding author on reasonable request.

Competing interests

The authors declare that they have no competing interests.

Funding

Support for the research reported, including assets and resources required for designing and performing experiments, data analysis, and interpretation, was provided by the National Institute of Environmental Health Sciences of the National Institutes of Health under Award Number (NIH grant # U24ES026946) as part of the Nanotechnology Health Implications Research (NHIR) Consortium. The content is solely the responsibility of the authors and does not necessarily represent the official views of the National Institutes of Health. The engineered nanomaterials used in the research presented in this publication were procured/developed, characterized, and provided by the Engineered Nanomaterials Resource and Coordination Core established at Harvard T. H. Chan School of Public Health (NIH grant # U24ES026946) as part of the Nanotechnology Health Implications Research Consortium. Partial financial support for DB was provided by the Harvard-Cyprus Endowment. This work was performed in part at the Harvard University Center for Nanoscale Systems (CNS), a member of the National Nanotechnology Coordinated Infrastructure Network (NNCI), which is supported by the National Science Foundation under NSF award no. ECCS-2025158.

Authors' contributions

LB contributed to experimental design, performed digestions and toxicity experiments, and co-wrote manuscript.

DB contributed to experimental design, performed characterization of 2DNMs, and co-wrote manuscript.

XC contributed to experimental design, performed digestions, and toxicity experiments.

GD contributed to experimental design and co-wrote manuscript.

DP synthesized materials performed characterization of pristine 2DNMs and co-wrote manuscript.

MS contributed to experimental design and data analysis

HYGL performed characterization of 2DNMs and co-wrote manuscript.

DCB contributed to data analysis and co-wrote manuscript.

BDT contributed to data analysis.

PD supervised study, contributed to experimental design and data analysis, and co-wrote manuscript.

Acknowledgements

Not applicable.

REFERENCES

1 S. Lanone and J. Boczkowski, *Eur. Respir. J.*, 2011, 37, 225–227.

2 G. Guisbiers, S. Mejía-Rosales and F. Leonard Deepak, *J. Nanomater.*, 2012, 2012.

3 M. Madhoushi, A. Malakani, G. Ebrahimi and A. Rashidi, *For. Wood Prod.*, 2020, **73**, 177–187.

4 A. Mohajerani, L. Burnett, J. V Smith, H. Kurmus, J. Milas, A. Arulrajah, S. Horpibulsuk and A. Abdul Kadir, *Materials (Basel).*, 2019, **12**, 3052.

5 P. Hassanzadeh, F. Atyabi and R. Dinarvand, *Biomed. Rev.*, 2018, **29**, 17–26.

6 K. Sampathkumar, S. Riyajan, C. K. Tan, P. Demokritou, N. Chudapongse and S. C. J. Loo, *ACS Omega*, , DOI:10.1021/acsomega.9b00823.

7 S. V. Pirela, J. Martin, D. Bello and P. Demokritou, *Crit. Rev. Toxicol.*, 2017.

8 D. Bello, J. Martin, C. Santeufemio, Q. Sun, K. Lee Bunker, M. Shafer and P. Demokritou, *Nanotoxicology*, , DOI:10.3109/17435390.2012.689883.

9 C. Luo, L. Zhou, K. Chiou and J. Huang, *Chem*, , DOI:10.1016/j.chempr.2018.02.021.

10 T. Xu, C. Ma, Z. Aytac, X. Hu, K. W. Ng, J. C. White and P. Demokritou, *ACS Sustain. Chem. Eng.*, , DOI:10.1021/acssuschemeng.0c02696.

11 P. S. Bindraban, C. O. Dimkpa, J. C. White, F. A. Franklin, A. Melse-Boonstra, N. Koele, R. Pandey, J. Rodenburg, K. Senthilkumar, P. Demokritou and S. Schmidt, *PLANTS, PEOPLE, PLANET*, , DOI:10.1002/ppp3.10098.

12 G. Pyrgiotakis, A. Vasanthakumar, Y. Gao, M. Eleftheriadou, E. Toledo, A. DeAraujo, J. McDevitt, T. Han, G. Mainelis and R. Mitchell, *Environ. Sci. Technol.*, 2015, **49**, 3737–3745.

13 Z. Aytac, R. Huang, N. Vaze, T. Xu, B. D. Eitzer, W. Krol, L. A. MacQueen, H. Chang, D. W. Bousfield and M. B. Chan-Park, *ACS Sustain. Chem. Eng.*, 2020, **8**, 15354–15365.

14 R. Huang, N. Vaze, A. Soorneedi, M. D. Moore, Y. Luo, E. Poverenov, V. Rodov and P. Demokritou, *Environ. Sci. Nano*, 2021, **8**, 514–526.

15 N. Vaze, G. Pyrgiotakis, L. Mena, R. Baumann, A. Demokritou, M. Ericsson, Y. Zhang, D. Bello, M. Eleftheriadou and P. Demokritou, *Food Control*, , DOI:10.1016/j.foodcont.2018.09.037.

16 M. Eleftheriadou, G. Pyrgiotakis and P. Demokritou, *Curr. Opin. Biotechnol.*, 2017, **44**, 87–93.

17 S. C. Sahu and A. W. Hayes, *Toxicol. Res. Appl.*, 2017, **1**, 239784731772635.

18 M. I. Setyawati, D. Singh, S. P. R. Krishnan, X. Huang, M. Wang, S. Jia, B. H. R. Goh, C. G. Ho, R. Yusoff, M. H. Kathawala, T. Y. Poh, N. A. T. B. M. Ali, S. H. Chotirmall, R. J. Aitken, M. Riediker, D. C. Christiani, M. Fang, D. Bello, P. Demokritou and K. W. Ng, *Environ. Sci. Technol.*, , DOI:10.1021/acs.est.9b06984.

19 Kenry and C. T. Lim, *ChemNanoMat*, 2017, **3**, 5–16.

20 K. Khan, A. K. Tareen, M. Aslam, R. Wang, Y. Zhang, A. Mahmood, Z. Ouyang, H. Zhang and Z. Guo, *J. Mater. Chem. C*, 2020, **8**, 387–440.

21 L. Ou, B. Song, H. Liang, J. Liu, X. Feng, B. Deng, T. Sun and L. Shao, *Part. Fibre Toxicol.*, 2016.

22 S. Priyadarsini, S. Mohanty, S. Mukherjee, S. Basu and M. Mishra, *J. Nanostructure Chem.*, 2018, **8**, 123–137.

23 M. Jedrzejczak-Silicka, M. Trukawka, M. Dudziak, K. Piotrowska and E. Mijowska, *Nanomaterials*, , DOI:10.3390/nano8080605.

24 R. Zhou, S. Zhu, L. Gong, Y. Fu, Z. Gu and Y. Zhao, *J. Mater. Chem. B*, 2019, 7, 2588–2607.

25 M. Alqahtani, *Materials (Basel).*, , DOI:10.3390/ma13102323.

26 A. Gracco, M. Dandrea, F. Deflorian, C. Zanella, A. De Stefani, G. Bruno and E. Stellini, *Nanomaterials*, , DOI:10.3390/nano9050753.

27 A. F. Khan, D. A. C. Brownson, E. P. Randviir, G. C. Smith and C. E. Banks, *Anal. Chem.*, 2016, **88**, 9729–9737.

28 Y. Feng, K. E. Marusak, L. You and S. Zauscher, *Curr. Opin. Colloid Interface Sci.*, 2018, 38, 190–203.

29 D. Singh, W. Wohlleben, R. De La Torre Roche, J. C. White and P. Demokritou, *NanoImpact*, , DOI:10.1016/j.impact.2018.12.003.

30 A. Kumar, P. Kumar, A. Anandan, T. F. Fernandes, G. A. Ayoko and G. Biskos, *J. Nanomater.*, 2014, 2014.

31 A. Boretti, S. Al-Zubaidy, M. Vaclavikova, M. Al-Abri, S. Castelletto and S. Mikhalovsky, *npj Clean Water*, 2018, 1, 1–11.

32 G. Fuertes, I. Soto, R. Carrasco, M. Vargas, J. Sabattin and C. Lagos, *J. Sensors*, 2016, 2016.

33 S. Kabiri, F. Degryse, D. N. H. Tran, R. C. Da Silva, M. J. McLaughlin and D. Losic, *ACS Appl. Mater. Interfaces*, 2017, **9**, 43325–43335.

34 D. Li, M. Morishita, J. G. Wagner, M. Fatouraie, M. Wooldridge, W. E. Eagle, J. Barres, U. Carlander, C. Emond and O. Jolliet, *Part. Fibre Toxicol.*, 2016, **13**, 45.

35 D. J. McClements, G. DeLoid, G. Pyrgiotakis, J. A. Shatkin, H. Xiao and P. Demokritou, *NanoImpact*, 2016, **3**–**4**, 47–57.

36 I. S. Sohal, K. S. O'Fallon, P. Gaines, P. Demokritou and D. Bello, *Part. Fibre Toxicol.*, 2018.

37 I. S. Sohal, G. M. DeLoid, K. S. O'Fallon, P. Gaines, P. Demokritou and D. Bello, *NanoImpact*, , DOI:10.1016/j.impact.2020.100209.

38 G. M. Deloid, X. Cao, R. M. Molina, D. I. Silva, K. Bhattacharya, K. W. Ng, S. C. J. Loo, J. D. Brain and P. Demokritou, *Environ. Sci. Nano*, , DOI:10.1039/c9en00184k.

39 Q. Yang, T. P. Keerthisinghe, T. R. J. Tan, X. Cao, M. I. Setyawati, G. DeLoid, K. W. Ng, S. C. J. Loo, P. Demokritou and M. Fang, *Environ. Sci. Nano*, 2020, **7**, 3155–3166.

40 C. Corbo, R. Molinaro, A. Parodi, N. E. Toledano Furman, F. Salvatore and E. Tasciotti, *Nanomedicine*, 2016, 11, 81–100.

41 S. Khare, G. M. DeLoid, R. M. Molina, K. Gokulan, S. P. Couvillion, K. J. Bloodsworth, E. K. Eder, A. R. Wong, D. W. Hoyt, L. M. Bramer, T. O. Metz, B. D. Thrall, J. D. Brain and P. Demokritou, *NanoImpact*, , DOI:10.1016/j.impact.2020.100216.

42 X. Cao, T. Zhang, G. M. DeLoid, M. J. Gaffrey, K. K. Weitz, B. D. Thrall, W.-J. Qian and P. Demokritou, *NanoImpact*, 2020, **20**, 100269.

43 I. L. Bergin and F. A. Witzmann, *Int. J. Biomed. Nanosci. Nanotechnol.*, , DOI:10.1504/IJBNN.2013.054515.

44 D. J. McClements, H. Xiao and P. Demokritou, *Adv. Colloid Interface Sci.*, 2017, **246**, 165–180.

45 D. J. McClements, F. Li and H. Xiao, *Annu. Rev. Food Sci. Technol.*, 2015, **6**, 299–327.

46 L. S. Costanzo and L. S. Preceded by: Costanzo, *Physiology*, Elservier, 6th edn., 2017.

47 R. Coreas, X. Cao, G. M. DeLoid, P. Demokritou and W. Zhong, *NanoImpact*, 2020, **20**, 100272.

48 I. S. Sohal, Y. K. Cho, K. S. O'Fallon, P. Gaines, P. Demokritou and D. Bello, *ACS Nano*, 2018.

49 Z. Guo, X. Cao, G. M. DeLoid, K. Sampathkumar, K. W. Ng, S. C. J. Loo and P. Demokritou, *J. Agric. Food Chem.*, 2019, **68**, 358–368.

50 A. Sukhanova, S. Bozrova, P. Sokolov, M. Berestovoy, A. Karaulov and I. Nabiev, *Nanoscale Res. Lett.*, 2018, 13.

51 X. Cao, G. M. G. M. Deloid, D. Bitounis, R. De La Torre-Roche, J. C. J. C. White, Z. Zhang, C. G. C. G. Ho, K. W. K. W. Ng, B. D. B. D. Eitzer and P. Demokritou, *Environ. Sci. Nano*, , DOI:10.1039/c9en00676a.

52 A. Pietroiusti, E. Bergamaschi, M. Campagna, L. Campagnolo, G. De Palma, S. Iavicoli, V. Leso, A. Magrini, M. Miragoli, P. Pedata, L. Palombi and I. Iavicoli, *Part. Fibre Toxicol.*, 2017, 14.

53 C. Fu, T. Liu, L. Li, H. Liu, Q. Liang and X. Meng, *Biomaterials*, 2015, **40**, 23–31.

54 E. Fröhlich and E. Roblegg, *Toxicology*, 2012, **291**, 10–7.

55 D. Bitounis, D. Parviz, X. Cao, C. A. Amadei, C. D. Vecitis, E. M. Sunderland, B. D. Thrall, M. Fang, M. S. Strano and P. Demokritou, *Small*, , DOI:10.1002/smll.201907640.

56 B. Liu, W. Qi, L. Tian, Z. Li, G. Miao, W. An, D. Liu, J. Lin, X. Zhang and W. Wu, *Nanoscale Res. Lett.*, 2015, **10**, 1–7.

57 B. Wu, L. Chen, X. Wu, H. Hou, Z. Wang and S. Liu, *Environ. Sci. Nano*, 2019, **6**, 1594–1606.

58 G. M. DeLoid, Y. Wang, K. Kapronezai, L. R. Lorente, R. Zhang, G. Pyrgiotakis, N. V. Konduru, M. Ericsson, J. C. White, R. De La Torre-Roche, H. Xiao, D. J. McClements and P. Demokritou, *Part. Fibre Toxicol.*, 2017, **14**, 40.

59 D. Parviz and M. Strano, *Curr. Protoc. Chem. Biol.*, 2018, **10**, e51.

60 Y. Duan, R. Coreas, Y. Liu, D. Bitounis, Z. Zhang, D. Parviz, M. Strano, P. Demokritou and W. Zhong, *NanoImpact*, , DOI:10.1016/j.impact.2020.100207.

61 K. J. Ong, T. J. MacCormack, R. J. Clark, J. D. Ede, V. A. Ortega, L. C. Felix, M. K. M. Dang, G. Ma, H. Fenniri, J. G. C. Veinot and G. G. Goss, *PLoS One*, , DOI:10.1371/journal.pone.0090650.

62 J. M. Wörle-Knirsch, K. Pulskamp and H. F. Krug, *Nano Lett.*, 2006, **6**, 1261–1268.

63 A. S. Wajid, S. Das, F. Irin, H. S. T. Ahmed, J. L. Shelburne, D. Parviz, R. J. Fullerton, A. F. Jankowski, R. C. Hedden and M. J. Green, *Carbon N. Y.*, 2012, **50**, 526–534.

64 R. Bari, D. Parviz, F. Khabaz, C. D. Klaassen, S. D. Metzler, M. J. Hansen, R. Khare and M. J. Green, *Phys. Chem. Chem. Phys.*, 2015, **17**, 9383–9393.

65 D. Parviz, F. Irin, S. A. Shah, S. Das, C. B. Sweeney and M. J. Green, *Adv. Mater.*, 2016, **28**, 8796–8818.

66 P. Ramalingam, S. T. Pusuluri, S. Periasamy, R. Veerabahu and J. Kulandaivel, *RSC Adv.*, 2013, **3**, 2369–2378.

67 J. Y. T. Chong, X. Mulet, L. J. Waddington, B. J. Boyd and C. J. Drummond, *Soft Matter*, 2011, **7**, 4768–4777.

68 S. R. Price, C. Kinnear and S. Balog, *Nanoscale*, 2019, **11**, 5209–5214.

69 B. Sun, Y. Zhang, Q. Liu, C. Yan, B. Xiao, J. Yang, M. Liu and L. Zhu, *Environ. Sci. Nano*, 2020, **7**, 634–644.

70 M. Lotya, A. Rakovich, J. F. Donegan and J. N. Coleman, *Nanotechnology*, , DOI:10.1088/0957-4484/24/26/265703.

71 M. C. Duch, G. R. S. Budinger, Y. T. Liang, S. Soberanes, D. Urich, S. E. Chiarella, L. A. Campochiaro, A. Gonzalez, N. S. Chandel and M. C. Hersam, *Nano Lett.*, 2011, **11**, 5201–5207.

72 G. M. Mutlu, G. R. S. Budinger, A. A. Green, D. Urich, S. Soberanes, S. E. Chiarella, G. F. Alheid, D. R. McCrimmon, I. Szleifer and M. C. Hersam, *Nano Lett.*, 2010, **10**, 1664–1670.

73 C. Martín, K. Kostarelos, M. Prato and A. Bianco, *Chem. Commun.*, 2019, **55**, 5540–5546.

74 R. Kurapati, C. Backes, C. Ménard-Moyon, J. N. Coleman and A. Bianco, *Angew. Chemie - Int. Ed.*, 2016, **55**, 5506–5511.

75 L. Liao, H. Peng and Z. Liu, *J. Am. Chem. Soc.*, 2014, **136**, 12194–12200.

76 Z. Wang, A. von dem Bussche, Y. Qiu, T. M. Valentin, K. Gion, A. B. Kane and R. H. Hurt, *Environ. Sci. Technol.*, 2016, **50**, 7208–7217.

77 E. P. Gray, C. L. Browning, M. Wang, K. D. Gion, E. Y. Chao, K. J. Koski, A. B. Kane and R. H. Hurt, *Environ. Sci. Nano*, 2018, **5**, 2545–2559.

78 G. Yang, S. Z. F. Phua, A. K. Bindra and Y. Zhao, *Adv. Mater.*, 2019, **31**, 1–23.

79 J. Hao, G. Song, T. Liu, X. Yi, K. Yang, L. Cheng and Z. Liu, *Adv. Sci.*, 2017, **4**, 1600160.

80 N. Strigul, A. Koutsospyros and C. Christodoulatos, *Ecotoxicol. Environ. Saf.*, 2010, **73**, 164–171.

81 O. Wasel and J. L. Freeman, *Toxics*, 2018, **6**, 66.

82 J. Li, L. M. Guiney, J. R. Downing, X. Wang, C. H. Chang, J. Jiang, Q. Liu, X. Liu, K. Mei and Y. Liao, *Small*, 2021, 2101084.

83 Z. Guo, G. M. DeLoid, X. Cao, D. Bitounis, K. Sampathkumar, K. W. Ng, S. C. J. Loo and P. Demokritou, *Environ. Sci. Nano*.

84 I. P. de Sousa, K. Buttenhauser, W. Suchaoin, A. Partenhauser, M. Perrone, B. Matuszczak and A. Bernkop-Schnürch, *Int. J. Pharm.*, 2016, **509**, 360–367.

TABLES

Table 1. Key physicochemical properties of 2DNM used in this study.

	2DNM	Lateral size (nm ± S.D.)	Mean thickness (nm)	C:O ratio	Dispersant / concentration (mg/ml)	Complete characterization
Graphene-related	Small-sized graphene oxide (GO-S)	271 ± 34*	0.77 ± 0.08	64:35	N/A	**Table S1**
	Medium-sized graphene oxide (GO-M)	462 ± 114*	0.94 ± 0.25	61:39	N/A	[55]
	Large-sized graphene oxide (GO-L)	1560 ± 750†	0.97 ± 0.25	61:38	N/A	[55]
	Small-sized reduced graphene oxide (rGO-S)	411 ± 79*	2.25 ± 1.85	78:22	Na-cholate / 5.0	[60]
	Large-sized reduced graphene oxide (rGO-L)	2015 ± 674†	62	78:22	Na-cholate / 2.5	**Table S2**
	Partially reduced graphene oxide (prGO)	357 ± 42*	3	72:28	Na-cholate / 4.0	**Table S3**
	Small-sized graphene in Na-cholate	184 ± 23*	5.86 ± 1.19	N/A	Na-cholate / 4.0	[60]
	Small-sized graphene in Pluronic F108	206 ± 51*	5	N/A	Pluronic F108 / 10.0	**Table S4**
Inorganic	Hexagonal boron nitride (hBN)	149 ± 12*	10	N/A	Na-cholate / 4.0	[60]
	Molybdenum disulphide (MoS_2)	428 ± 103*	5	N/A	Na-cholate / 5.0	[60]
	Tungsten disulphide (WS_2)	323 ± 28*	6	N/A	Pluronic F108 / 10.0	**Table S5**

* mean lateral size and S.D. extrapolated by the hydrodynamic size distribution of the sample as measured by single-particle trackign and after aplicaiton of an algorithm by Lotya et al. [70];
† mean lateral size and S.D. extrapolated by AFM measuremetns.

Table 2. Summary of colloidal properties of 2DNM-enabled fasting food models at 250 μg/ml.

	2DNM-enabled fastign food models	**z-average (nm ± S.D.)**	**pdi (± S.D.)**	**z-potential (mV ± S.D.)**	**diffusion coefficient ($\mu m^2/s$ ± S.D.)**
Graphene-related	Small-sized graphene oxide (GO-S)	183 ± 2	0.2 ± 0.0	-47.0 ± 4.0	2.7 ± 0.0
	Medium-sized graphene oxide (GO-M)	282 ± 4	0.3 ± 0.0	-45.0 ± 1.0	1.7 ± 0.0
	Large-sized graphene oxide (GO-L)	822 ± 25	0.4 ± 0.0	-44.0 ± 2.0	0.6 ± 0.0
	Small-sized reduced graphene oxide (rGO-S)	308 ± 5	0.3 ± 0.1	-37.0 ± 1.0	1.6 ± 0.0
	Large-sized reduced graphene oxide (rGO-L)	533 ± 10	0.4 ± 0.1	-43.0 ± 2.0	0.9 ± 0.0
	Partially reduced graphene oxide (prGO)	193 ± 2	0.2 ± 0.0	-41.0 ± 2.0	2.6 ± 0.0
	Small-sized graphene in Na-cholate	139 ± 11	0.3 ± 0.1	-42.0 ± 0.0	3.6 ± 0.3
	Small-sized graphene in Pluronic F108 (g-PF108-S)	194 ± 3	0.2 ± 0.0	-16.0 ± 1.0	2.5 ± 0.1
Inorganic	Hexagonal boron nitride (hBN)	80 ± 1	0.2 ± 0.0	-42.0 ± 3.0	6.2 ± 0.1
	Molybdenum disulphide (MoS_2)	494 ± 12	0.3 ± 0.1	-35.0 ± 1.0	1.0 ± 0.0
	Tungsten disulphide (WS_2)	187 ± 2	0.2 ± 0.0	-42.0 ± 0.0	3.6 ± 0.3

pdi: polydisperisty index.

FIGURE LEGENDS

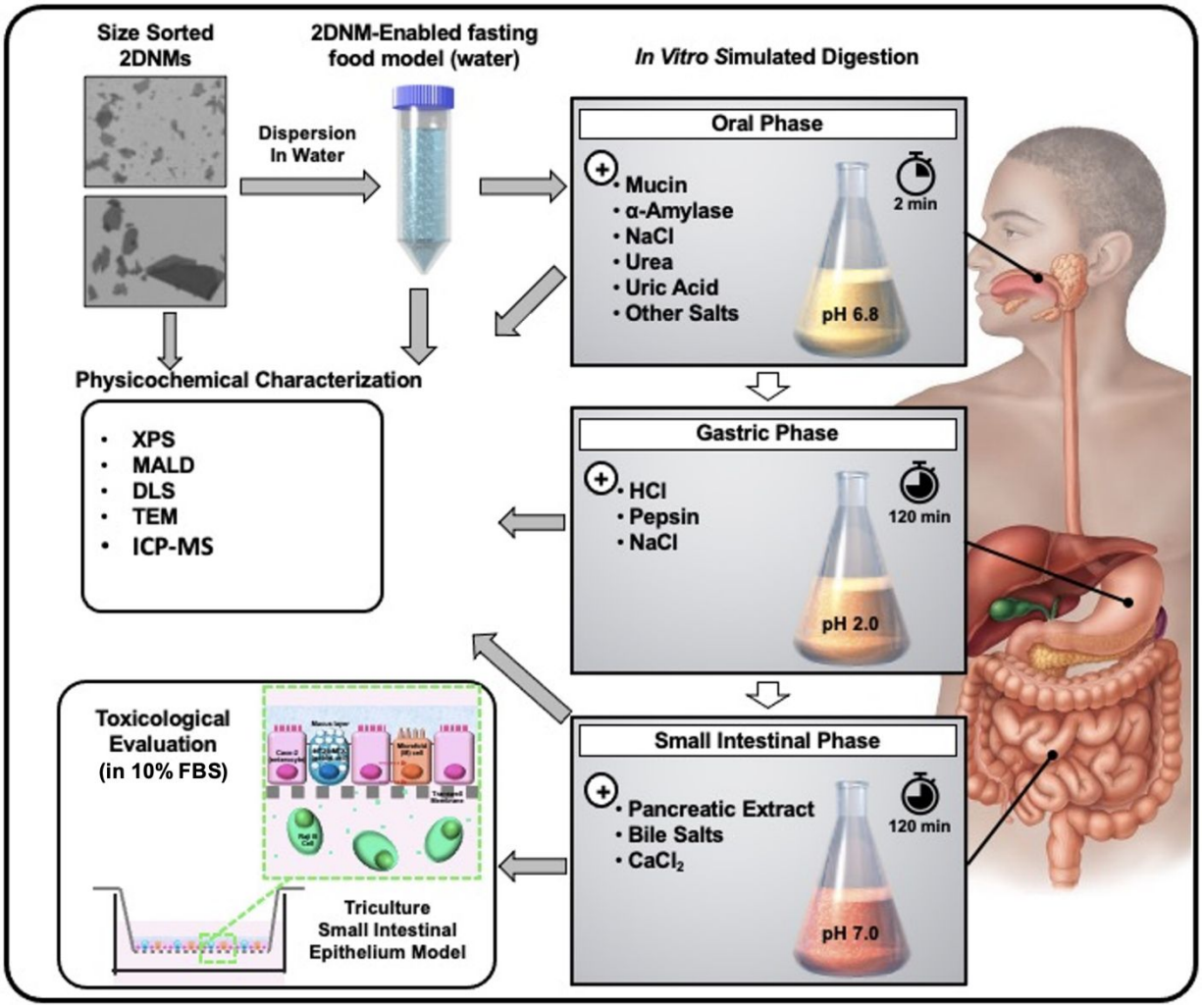

Figure 1. Schematic diagram of the study design. This study presents the preparation of 2DNM-enabled fasting food model and exposing them to a GIT simulated digestion which consists of (from top to bottom) a mouth, stomach, and small intestinal phase. Physicochemical characterization of the 2DNMs is carried out along with their toxicological assessment against an *in vitro* Triculture model representing the human small intestinal epithelium.

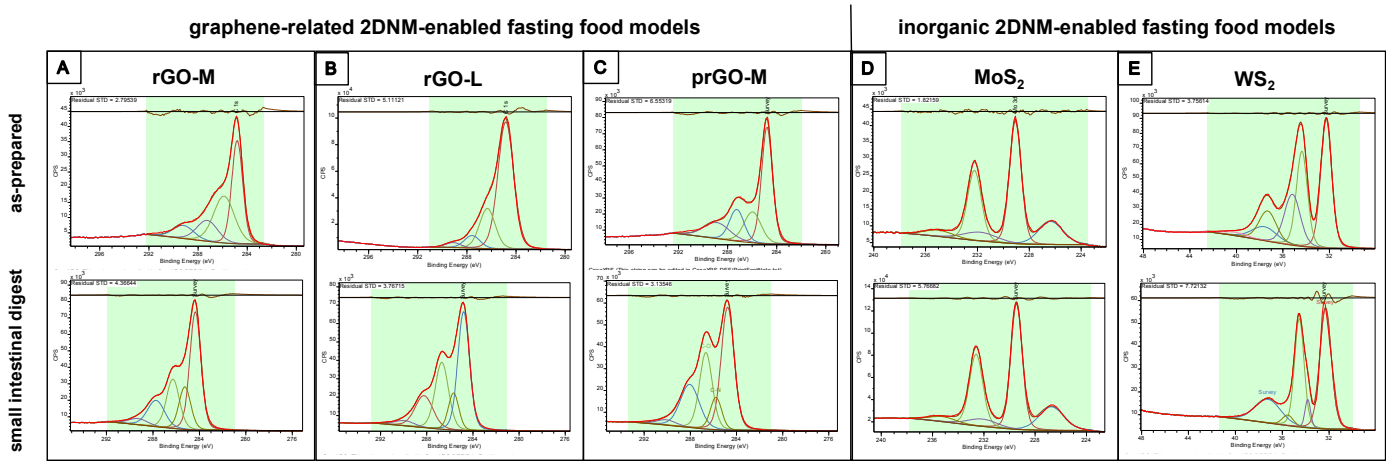

Figure 2. **Surface chemistry analyses of 2DNM-enabled fasting food models before and after simulated digestion.** The XPS spectra of 2DNM-enabled fasting food models prior to and after digestion are presented in the top and bottom row, respectively. **(A)** rGO-S, **(B)** rGO-L, **(C)** prGO, **(D)** MoS_2, and **(E)** WS_2.

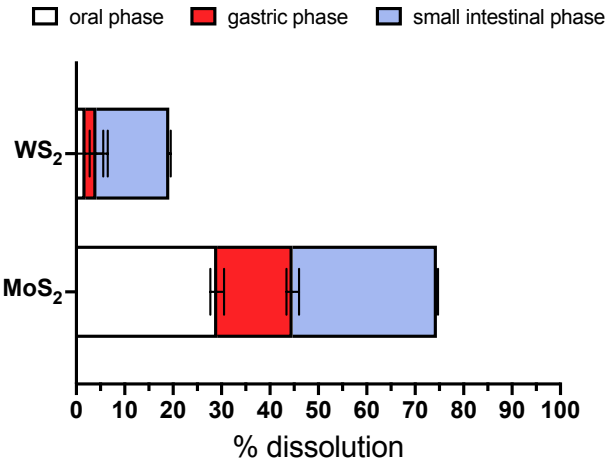

Figure 3. Evaluation of dissolution of **(A)** MoS_2- and **(B)** WS_2-enabled fasting food models during simulated digestion as measured by ICPMS. Error bars represent S.D.; N=3.

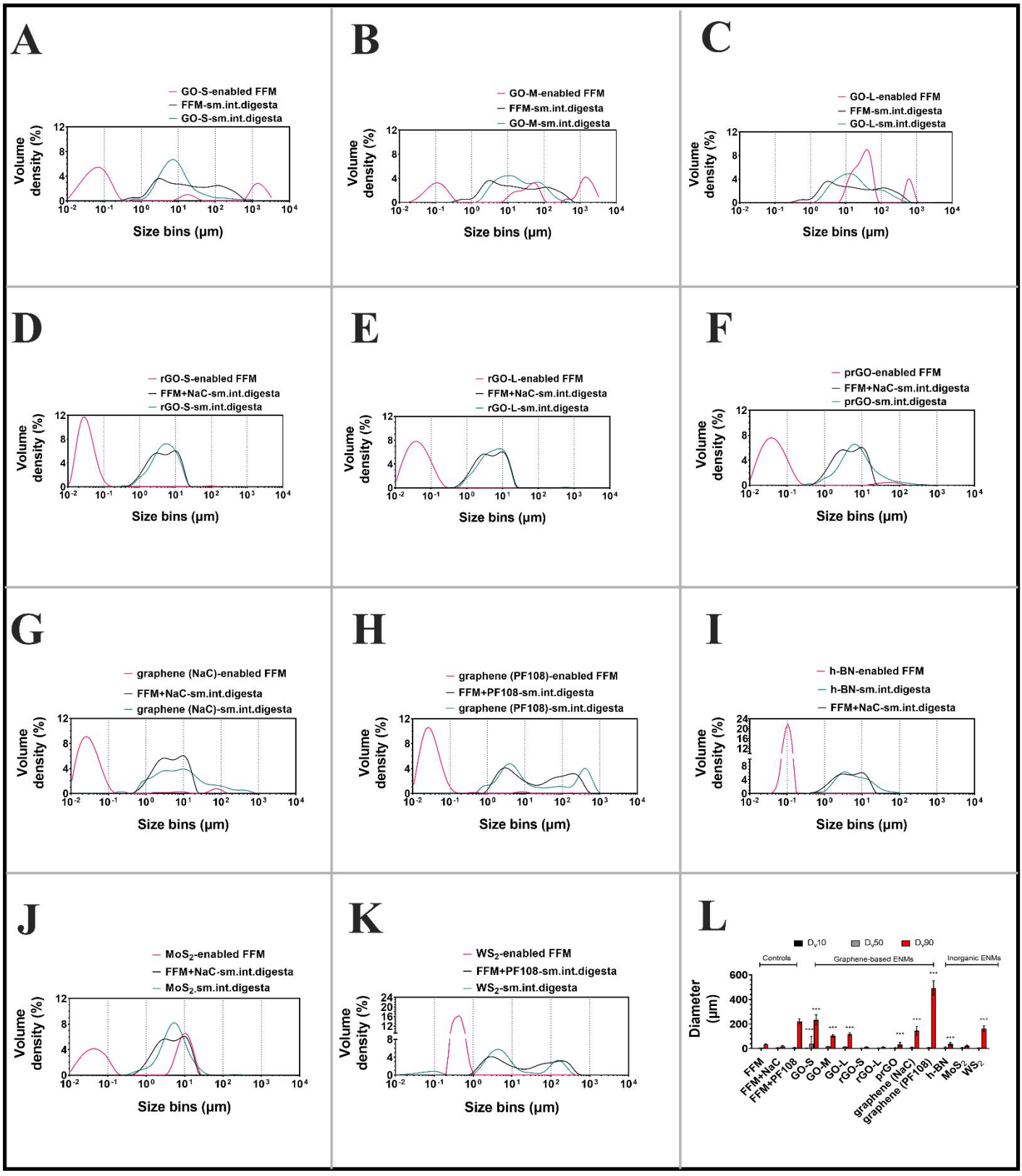

Figure 4. Volume-weighted size distributions of graphene-based and inorganic nano-enabled FFM and their small intestinal digestas using MALD. A-K. Volume-weighted size distributions of GO-S, GO-M, GO-

L, rGO-S, rGO-L, prGO, graphene (Na-cholate), MoS_2, h-BN, WS_2, graphene (PF108)-enabled FFMs and small intestine digestas, respectively. Each panel also presents their control blank digestas: FFM, FFM+Na-cholate at 8 mg/ml, or FFM+PF108 at 7.8 mg/ml. **L.** Dv_{10}, Dv_{50} and Dv_{90} values (values below which lie 10%, 50% and 90% of a sample's cumulative particle volume, respectively) for the small intestinal digestas and blank controls of GO-S, GO-M, GO-L, rGO-S, rGO-L, prGO, graphene (Na-cholate), MoS_2, h-BN, WS_2, and graphene (PF108). Statistical analyses were performed using Tukey's test (multiple comparisons); *p < 0.05, *** p <0.001.

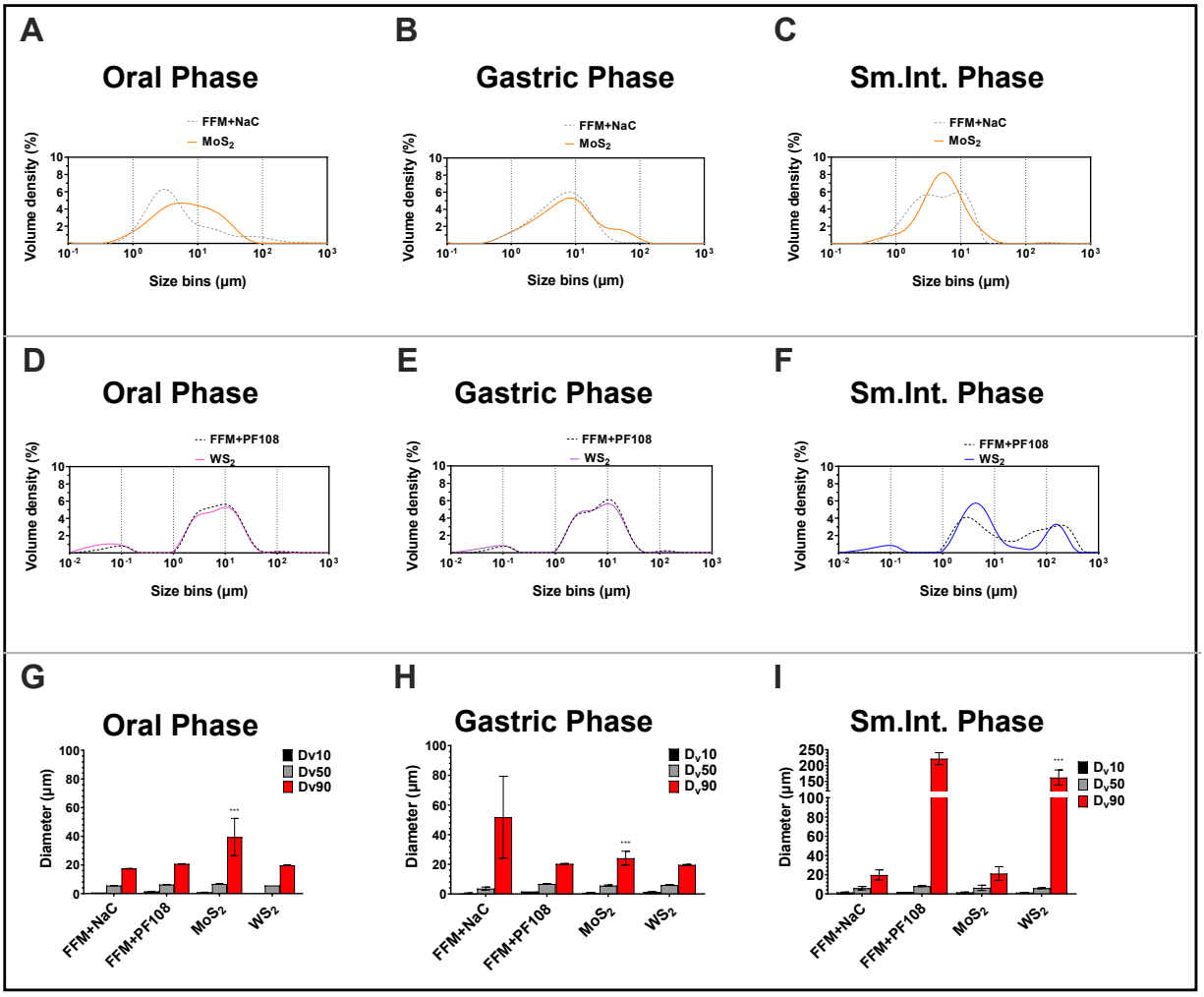

Figure 5. Volume-weighted size distributions of MoS_2- and WS_2-enabled FFM digestas across the oral, gastric, and small intestinal phase. Volume-weighted size distributions across the oral, gastric, and small intestinal phase for **(A-C)** MoS_2- and **(D-F)** WS_2-enabled FFMs. Each panel also presents their control blank

digestas: FFM, FFM+Na-cholate at 8 mg/ml, or FFM+PF108 at 7.8 mg/ml. digestas and FFM+Na-cholate (Na-cholate alone at a starting concentration of 8 mg/ml). **(G-I)** D_v10, D_v50 and D_v90 values (values below which lie 10%, 50% and 90% of a sample's cumulative particle volume, respectively) for MoS_2- and WS_2-enabled FFM in the oral, stomach and small intestinal digestas, respectively.

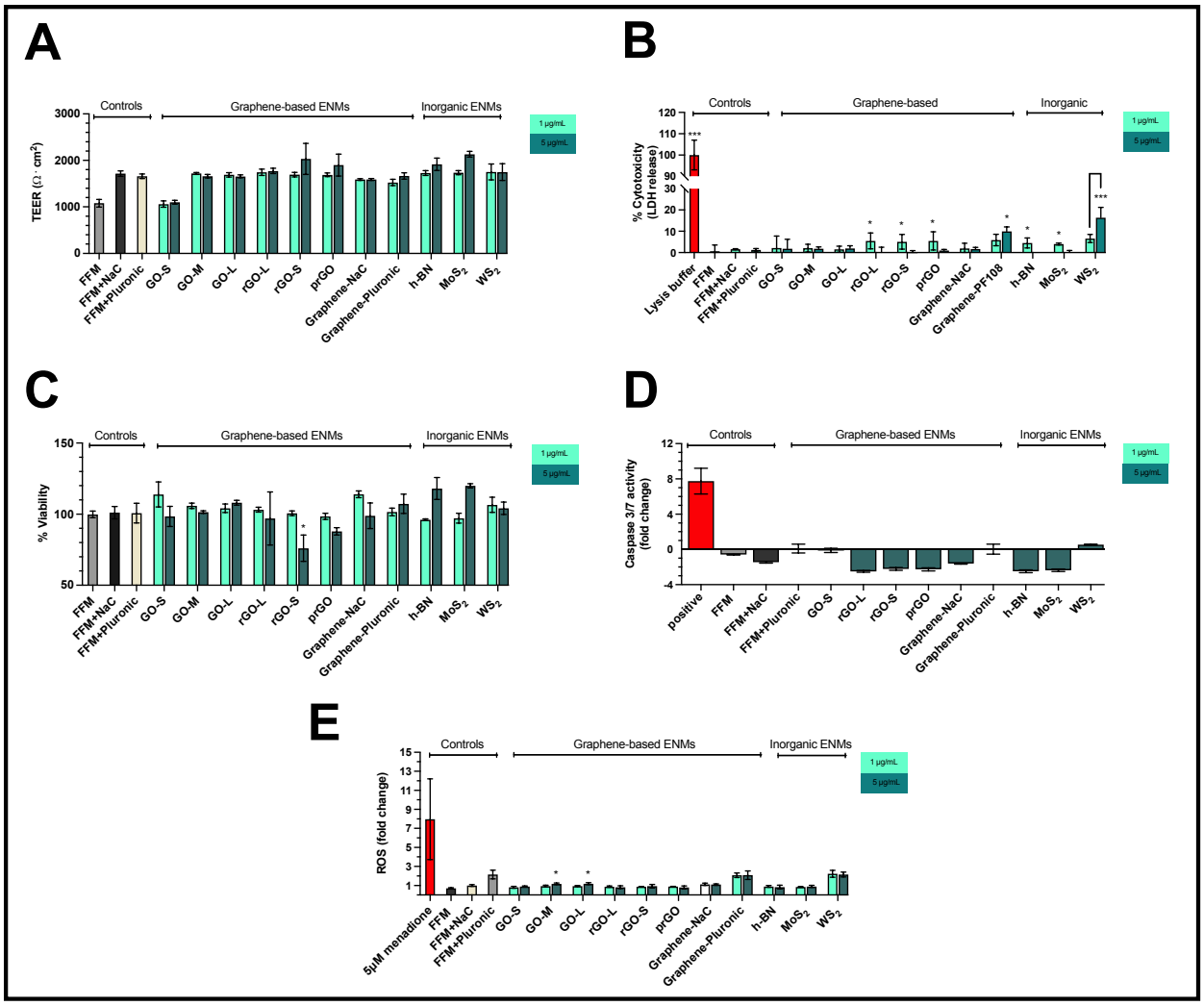

Figure 6. ***In vitro*** **toxicological assessment of graphene based and inorganic 2DNMs in tri-cultures and co-cultures exposed to small intestinal digestas.** Results of toxicological assessments of GO-S, GO-M, GO-L, rGO-S, rGO-L, prGO, graphene-Na-cholate, and graphene-PF108, h-BN, MoS_2 and WS_2-enabled FFMs small intestine digestas **A** TEER values (expressed as Ω cm^2) after 24-hour exposure. **B.** Cytotoxicity (LDH release)

calculated as % of LDH in lysed control (24-hour exposure). **C** Cell viability (mitochondrial enzymatic activity) expressed as % of activity (fluorescence) measured in cells treated with control FFM digesta (24-hour exposure). **D** Caspase 3/7 activity (apoptosis) after 24-hour exposure expressed as fold change relative to that in cells exposed to FFM digesta (24-hour exposure). **E** ROS generation expressed as fold change relative to that in cells exposed to FFM digesta (measured after 6-hour exposure). In the controls group, positive controls are depicted in red, whereas the rest represent negative (untreated) controls. All digestions and exposures were performed in triplicate. Error bars represent mean ± standard deviation. * $p < 0.05$; *** $p < 0.001$.